An *ab initio* Study on the Mechanical Stability, Spin-Dependent Electronic Properties, Molecular Orbital Predictions, and Optical Features of Antiperovskite A₃InN (A = Co, Ni)

Al Momin Md Tanveer Karim,* Md Jubair, Md Nuruzzaman, and Md Abdul Kader Zilani*

ACCESS | Metrics & More | Article Recommendations

ABSTRACT: Structural, mechanical, spin-dependent electronic, magnetic, and optical properties of antiperovskite nitrides A₃InN (A = Co, Ni) along with molecular orbital diagram are investigated here by using an *ab initio* density functional theory (DFT). The mechanical stability, deformation, damage tolerance and ductile nature of A₃InN are confirmed from elastic calculations. Different mechanical anisotropy factors are also discussed in detail. The spin dependent electronic properties such as the band structure and density of states (DOS) of A₃InN are studied and, the dispersion curves and DOS at Fermi level are different for up and down spins only in case of Co₃InN. These calculations also suggest that Co₃InN and Ni₃InN behave as ferromagnetic and nonmagnetic, respectively. The induced total magnetic moment of Co₃InN is

found 2.735 μ_B/cell in our calculation. Mulliken bond population analysis shows that the atomic bonds of A₃InN are contributed by both ionic and covalent bonds. Molecular orbital diagrams of A₃InN antiperovskites are proposed by analyzing orbital projected band structures. The formation of a molecular orbital energy diagram for Co₃InN is similar to Ni₃InN with respect to hybridization and orbital sequencing. However, the orbital positions with respect to the Fermi level (E_F) and separations between them are different. The Fermi surface of A₃InN is composed of multiple nonspherical electron and hole type sheets in which Co₃InN displays a spin-dependent Fermi surface. The various ground-state optical functions such as real and imaginary parts of the dielectric constant, optical conductivity, reflectivity, refractive index, absorption coefficient, and loss function of A₃InN are studied with implications. The reflectivity spectra reveal that A₃InN reflects >45% of incident electromagnetic radiations in both the visible and ultraviolet region, which is an ideal feature of coating material for avoiding solar heating.
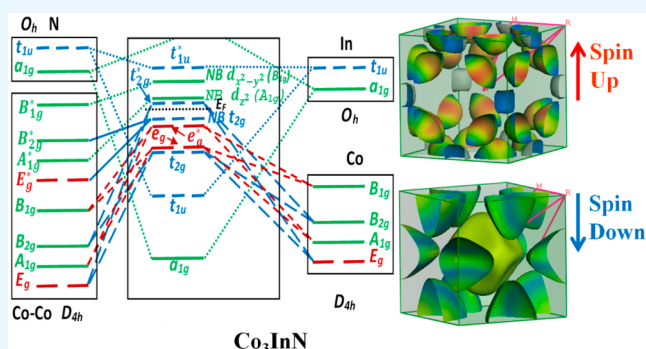
1. INTRODUCTION

Antiperovskite transition-metal nitrides (ATMNs) have become familiar to scientists and researchers in the last several decades.[1−3] ATMNs demonstrate a broad range of attractive and tunable physical properties such as the Invar-like effect, itinerant antiferromagnetism, giant magneto-resistance, super-conductivity, damage tolerance, spin-glass-like activities, strong spin−lattice coupling characteristics, and topological electronic behavior.[1,4−8] Perovskite compounds are denoted by the formula ABX₃, where A and B are cations and X is an anion. In antiperovskite compounds, the general formula is reversed, so that the X sites are occupied by a cation, while A and B sites are occupied by different types of anions. Typical ATMNs adopt the crystal structure A₃BX with space group $Pm\overline{3}m$ (no. 221), where A is a transition metal; B is a divalent or trivalent element; and X is nitrogen.[4,5] B. V. Beznosikov predicted more than 80 nitride compounds with antiperovskite structure.[9] The generation of large negative thermal expansion in Ge-doped antiperovskite manganese nitrides Mn₃XN (X = Cu, Zn, Ga) is reported by

Takagi et al.[10] Ferro- and paramagnetic orders are observed in ATMNs when the transition elements are substituted by group 13 metals.[11,12] It is reported that the nonstoichiometry affects the magnetic properties in Ni-rich antiperovskite carbides depending on Ni/C atomic ratios.[13−15] However, the non-magnetic ground state is found in many cases for Ni-based ternary carbides due to the reduced Stoner factor and C−Ni bonding nature.[16−18] Although there are predictions about some highly stable two-dimensional (2D) hypercoordinate materials such as Cu−Si and Cu−Ge alloy films, Ni₂Ge and Ni₂Si monolayers, aluminum boride (AlB₆) nanosheets with interest-

ing physical properties, and diverse applications,[19−26] here we consider only the bulk antiperovskite A$_3$InN in our calculation.

The nickel (Ni)-based antiperovskite nitrides gained considerable interest due to the discovery of superconductivity in Ni$_3$CuN and Ni$_3$ZnN with T_C around 3 K.[27,28] Ni$_3$CdN exhibits very soft and weak ferromagnetism, and Ni$_3$InN exhibits a spin−glass-like behavior.[29,30] Different groups synthesized Co$_3$InN and Ni$_3$InN by different methods.[1−4] Due to the diversity of the physical properties of the antiperovskite materials and limited knowledge on the cobalt- and Ni-based nitrides, first-principle calculations for Co$_3$InN and Ni$_3$InN were carried out in order to study shear, Young's moduli, Poisson's ratio, and spin-polarized band structure and projected density of states (pDOS) only.[3] To extend these previous works, we thus focus here on exposing different physical properties of Co- and Ni-based antiperovskite A$_3$InN (A = Co, Ni) nitrides using an *ab initio* density functional theory (DFT) method. The spin-polarized structural, elastic, and mechanical stability and the effect of spin in electronic behavior, magnetic nature, bonding character, and optical properties of antiperovskites A$_3$InN are elucidated in detail. In addition, to expose the strength and extent of anisotropy of A$_3$InN, we focused on the Vickers hardness and different anisotropy indices, respectively. The anisotropic mechanical behavior and elastic responses of A$_3$InN are presented by two- and three-dimensional graphical presentations. To take full advantage of the electronic properties of A$_3$InN in addition to spin-polarized bands and pDOS, we represent here the results of magnetic moments (total and individual atoms), charge density distribution mapping, and spin-polarized Fermi surface topologies. The Fermi surface can provide information for predicting the physical properties of a metal.

The molecular orbital (MO) theory is regarded as an effective tool to determine the molecular structure and bonding nature of a compound. It takes the idea of overlapping between different atomic orbitals. The distribution of different MO energy levels is represented by a MO diagram. It also gives insight about bonding, bond order, and change of molecular behavior with ionization. A lot of reports are published on the MO diagram for ternary X$_2$YZ Heusler compounds,[31,32] where X and Y are transition metals and Z is a main group element. Compared to X$_2$YZ Heusler compounds, the study of d-orbital hybridization and bonding order for A$_3$BX-based antiperovskite has not been explored yet to the best of our knowledge.

Moreover, we predicted the orbital hybridization among different atoms based on orbital-projected band diagrams and unfolding orbital degeneracy of A$_3$InN which may help to better understand the magnetic behavior of these compounds.

Finally, the interaction of A$_3$InN with electro-magnetic radiation is expressed by means of some nonlinear optical constants such as reflectance, absorption coefficient, refractive index, complex dielectric constants, optical conductivity, and loss function. As far as we know, there are no experimental or theoretical data available on the Vickers hardness, anisotropic elastic indices, Fermi surface topology, and nonlinear optical properties of A$_3$InN, which are focused here. We strongly believe this study will be useful for using A$_3$InN in the arena of engineering applications.

2. METHODS OF CALCULATIONS

The ground-state physical properties of the A$_3$InN (A = Co and Ni) are simulated using *ab initio* density functional theory (DFT) via the CASTEP code.[33] The Vanderbilt-type ultrasoft pseudopotential method is employed to treat the outermost electrons as valence electrons for each atom in A$_3$InN. The Perdew−Burke−Ernzerhof (PBE) parametrization within the generalized gradient approximation (GGA) is applied to treat the exchange and correlation interactions.[34] The plane-wave cutoff energy of 500 eV is used to expand the Eigen functions of the valence and nearly valence electrons. The Monkhorst−Pack grid of $18 \times 18 \times 18$ k-points is used to investigate the Brillouin zone. The Broyden−Fletcher−Goldferb−Shanno (BFGS) algorithm is employed to optimize the geometry optimization through minimizing the total energy and the internal forces.[35] To optimize the geometry conditions, the tolerances for total energy, maximum force, maximum stress, and maximum atomic displacement are set to less than 5×10^{-6} eV per atom, 0.01 eV/ Å, 0.02 GPa, and 5×10^{-4} Å, respectively. The single-crystal elastic tensors (C_{ij}) are calculated by the "stress−strain" method embedded into the CASTEP code in which a set of finite identical deformations is applied. The resultant stress is calculated after optimization of the internal degrees of freedom, and a maximum amplitude of 0.003 Å is chosen for each strain having four steps. The atomic population analysis is performed by means of the conventional Mulliken formalism. The electron charge density difference and Fermi surface are calculated by setting the k-point separation to less than 0.01 Å^{-1} with $26 \times 26 \times 26$ grids. The optical properties of A$_3$InN are calculated using the same code. It is important to note that spin polarization is considered in all calculations. Orbital-projected band diagrams of these compounds A$_3$InN (A = Co and Ni) are also evaluated using the Quantum ESPRESSO[36] code with the above motioned parameters.

3. RESULTS AND DISCUSSION

3.1. Structural Properties. Bulk A$_3$InN (A = Co and Ni) is crystallized as a cubic system in space group $Pm\bar{3}m$ (no. 221).[1] The crystal structure of antiperovskite A$_3$InN nitrides in the above-mentioned space group is shown in Figure 1. The
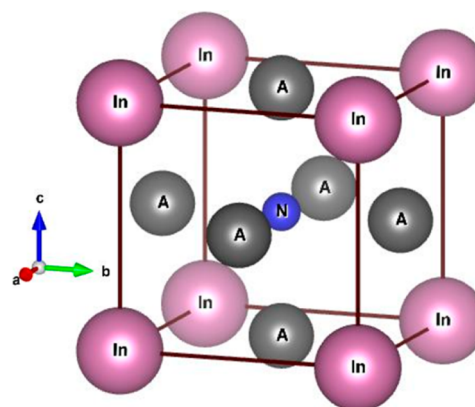

Figure 1. Crystal structure of A$_3$InN (A = Co and Ni) ternary antiperovskites.

structural unit cell of A$_3$InN, which adopts an octahedral coordinate, consists of six A atoms, one In atom, and one N atom. The Wyckoff positions are at (0, 1/2, 1/2), (0, 0, 0), and (1/2, 1/2, 1/2) for A, In, and N atoms, respectively. The equilibrium crystal structures of A$_3$InN are optimized at the minimum total energy. The calculated lattice parameter and unit cell volume of A$_3$InN are tabulated in Table 1. It is observed that the lattice constants of A$_3$InN which are very close (<1.07%)

compared to the experimental values[1,4] indicate the highest level of accuracy of our study.

Table 1. Comparison between the Theoretically Calculated and Experimental Values of Unit Cell Parameters of A_3InN (A = Co, Ni)[a]

phase	a (Å)	V (Å)³	method	reference
Co_3InN	3.877	58.287	DFT (GGA)	this work
Ni_3InN	3.901	59.361	DFT (GGA)	this work
Co_3InN	3.855	57.289	DFT (GGA)	3
	3.753	52.861	DFT (LDA)	
Ni_3InN	3.882	58.501	DFT (GGA)	3
	3.784	54.181	DFT (LDA)	
Co_3InN	3.8518	57.146	electrochemical bulk synthesis	1
Ni_3InN	3.8599	57.509	electrochemical bulk synthesis	1
Co_3InN	3.8541	57.249	solid−gas reactions	4
Ni_3InN	3.8445	56.822	solid−gas reactions	4

[a]GGA = generalized gradient approximation. LDA = local density approximation. FM = ferromagnetic. NM = Nonmagnetic.

3.2. Mechanical Properties. The mechanical properties are important because they describe different characteristics such as elasticity, plasticity, strength, hardness, ductility, and brittleness of a material. Among these properties elastic constants correlate the dynamical behavior of a material with its mechanical properties. The single-crystal elastic tensors (C_{ij}) of newly synthesized A_3InN (A = Co, Ni) are calculated to provide a deep insight into the mechanical stability and stiffness of these materials. In general, materials with cubic symmetry have three adiabatic elastic stiffness constants, namely, C_{11}, C_{12}, and C_{44}. The constant C_{11} is related to tensile, whereas C_{12} and C_{44} are associated to share. The values of C_{11}, C_{12}, and C_{44} are listed in Table 2. The elastic constants of A_3InN satisfy the Born stability[37] criteria $C_{11} > 0$, $C_{11} - C_{12} > 0$, $C_{44} > 0$, and ($C_{11} + 2C_{12}$) > 0 signifies the mechanical stability for these cubic crystals. It has also been seen that the constants follow $C_{11} > C_{12} > C_{44}$, which indicates the anisotropic nature, whereas the low value of C_{44} is allied to the shear deformation and damage-tolerant nature of A_3InN. The different elastic moduli (B, G, Y, and ν) are also calculated from individual elastic constants. The bulk modulus (B) of A_3InN is given by

$$B = \frac{C_{11} + 2C_{12}}{3} \tag{1}$$

The shear modulus (G) of a crystalline solid varies with direction and is defined by the Voigt−Reuss−Hill (VRH) equation as

$$G_V = \frac{1}{5}(C_{11} - C_{12} + 3C_{44}) \tag{2}$$

$$G_R = \frac{5(C_{11} - C_{12})C_{44}}{4C_{44} + 3(C_{11} - C_{12})} \tag{3}$$

where G_V and G_R are the Voigt and Reuss bonds, respectively. The arithmetic average of G_V and G_R gives the shear modulus of A_3InN.

$$G = \frac{G_V + G_R}{2} \tag{4}$$

The isotropic polycrystalline aggregate values for Young's modulus (E) and Poisson's ratio (ν) are obtained using the following equations as

$$Y = \frac{9GB}{(G + 3B)} \tag{5}$$

$$\nu = \frac{3B - 2G}{2(3B + G)} \tag{6}$$

The values of B, G, Y, and ν are tabulated in Table 2. In general, the hardness of a compound is measured by B and G. The values of B (G) are found to be 197 (93) GPa and 182 (63) GPa for Co_3InN and Ni_3InN, respectively, indicating higher hardness of Co_3InN. Moreover, the high value of the bulk modulus with low shear modulus reveals the damage-tolerant, quasi-ductile, easily machinable, and stiff nature of A_3InN. On the other hand, Co_3InN is found to be stiffer than Ni_3InN due to the higher value of Y. Another three important factors, Poisson's ratio (ν), Pugh's ratio (G/B), and Cauchy pressure ($C_{12} - C_{44}$), have also been calculated and shown in Table 2. From Table 2, it is seen that ν is greater than Frantsevich's criterion[38] value of 0.26 and G/B < 0.57. These parameters suggest that A_3InN is ductile. The elastic nature of A_3InN is also verified by the Cauchy pressure.[39] The negative value of Cauchy pressure indicates the brittle nature of the compound, while a positive value endorses the quasi-ductile nature. In addition, the values of B, G, Y, ν, G/B, and ($C_{12} - C_{44}$) are compared with other antiperovskites and found to be consistent, which is shown in Table 2.

The Vickers hardness (H_V) is highly related to the elastic constants of a material. We have calculated the H_V of A_3InN using the different approximations proposed by Teter et al.,[40] $(H_V)_{Teter}$ = 0.151 G, Tian et al.,[41] $(H_V)_{Tian}$ = $0.92(G/B)^{1.137}G^{0.708}$, and Chen et al.,[42] $(H_V)_{Chen}$ = $2[(G/B)^2 G]^{0.585}$ − 3. The calculated values of H_V are presented in Table 3. It is noticeably seen that Co_3InN has higher H_V than Ni_3InN which may be due to a higher elastic moduli and bond strength.

Mechanical anisotropy is closely related to different essential physical processes of a material. To visualize the level of anisotropic mechanical behavior and elastic responses of A_3InN, theYoung's modulus (Y), linear compressibility (β), shear modulus (G), and Poisson's ratio (ν) are plotted in contour plots

Table 2. Comparison of Elastic Properties between A_3InN (A = Co, Ni) and Other Antiperovskites

compound	C_{11}	C_{12}	C_{44}	B	G	Y	ν	G/B	$C_{12} - C_{44}$	ref
Co_3InN	333	129	87	197	93	241	0.29	0.472	42	this work
Co_3InN	317	126	95	190	95	224	0.28	0.50	31	3[a]
Ni_3InN	283	131	55	182	63	170	0.34	0.346	76	this work
Ni_3InN	274	131	60	178	64	172	0.34	0.359	71	3[a]
Ti_3TlN	196	131	52	153	43	118	0.40	0.276	79	8[a]
Ni_3SnN	266	132	41	177	50	137	0.37	0.282	91	8[a]
Co_3AlC	451	119	86	230	112	290	0.29	0.487	38	8[a]

[a]Theoretical.

Table 3. Calculated Vickers Hardness (H_V) of A$_3$InN (A = Co, Ni)^a

compound	$(H_V)_{Teter}$	$(H_V)_{Tian}$	$(H_V)_{Chen}$	H_{Gao}	ref
Co$_3$InN	14.043	9.701	8.781		this work
Ni$_3$InN	9.513	5.174	3.525		this work
Ti$_3$TlN				3.6	8
Ni$_3$SnN				3.58	8
Co$_3$AlC				4.0	8
Ti$_3$AlC				7.8	43 [exptl]

^{a}The results of other antiperovskite compounds are listed for comparison.

of three- (3D) and two-dimensional (2D) presentations (Figures 2 and 3) using the ELATE code.[44] From Figures 2 and 3, it is demonstrated that all the constants except linear compressibility are deviated from the complete spherical (3D) and circular (2D) shapes, indicating the anisotropic nature of these compounds. However, the deviation from the spherical and circular shapes is the same in all directions (*xy*, *xz*, and *yz* planes) but a bit higher for Co$_3$InN compared to Ni$_3$InN. The maximum and minimum values of Y, β, G, and ν are enlisted in Table 4.

The elastic anisotropy of cubic A$_3$InN can be expressed using the Zener anisotropy factor[46] A_Z as

$$A_Z = \frac{2G(1 + \nu)}{Y} = \frac{2C_{44}}{C_{11} - C_{12}} \tag{7}$$

The Zener anisotropy factor is related to share anisotropy, and $A_Z = 1$ for a perfect elastically isotropic material.

An alternative measure of the elastic anisotropy (A_G) for the cubic compound is proposed by Chung and Buessem[47] as

$$A_G = \frac{3(A_Z - 1)^2}{3(A_Z - 1)^2 + 25A_Z} \tag{8}$$

The anisotropy factor A_G is expressed in percentage, and $A_G = 0$ indicates the isotropic nature of a material.

The universal elastic anisotropy index (A_U)[48] involves all the individual components of the elasticity tensor of a material which may be defined for a cubic crystal as

$$A_U = 5\frac{G_V}{G_R} - 5 \tag{9}$$

The logarithmic universal Euclidean anisotropy (A_L)[49] for a cubic compound is related to the Voigt and Reuss bounds on the bulk modulus simplifies as

$$A_L = \sqrt{5} \ln\left(\frac{G_V}{G_R}\right) \tag{10}$$

The orientation of Poisson's ratio is specified in two directions; the lateral contraction/extension in one direction and the corresponding extension/contraction in a normal direction. In general, the extreme values of Poisson's ratio may occur due to strain along $\langle 110 \rangle$ and the corresponding orthogonal strain along $\langle 001 \rangle$ and $\langle 110 \rangle$ for a cubic compound.[50] The extrema of Poisson's ratio in these particular directions is expressed as

$$\nu(110, 001) = \frac{2A_Z C_{12}}{3B + A_Z C_{11}} \tag{11}$$

$$\nu(110, 1\bar{1}0) = \frac{3B - A_Z C_{11}}{3B + A_Z C_{11}} \tag{12}$$

The values of A_Z, A_U, and A_L, $\nu(110, 001)$ and $\nu(110, 1\bar{1}0)$, are listed in Table 5. From the table it is clear that the values of different anisotropy parameters except A_Z are higher for Co$_3$InN than Ni$_3$InN. The zero value of A_U and A_L signifies the higher isotropic nature of Co$_3$InN than Ni$_3$InN. However, these anisotropy parameters confirm that Co$_3$InN is more anisotropic in compression, whereas Ni$_3$InN is more anisotropic in share. The extrema of Poisson's ratio is found, $\nu(110, 1\bar{1}0) > \nu(110, 001)$, which reveals that the orthogonal strain may occur along this particular direction for A$_3$InN.

3.3. Band Structure and Density of States (DOS). The electronic band structure and density of states (DOS) play an imperative role to visualize several optoelectrical and magnetic properties of a crystal at the microscopic level. The spin-polarized electronic band structures of A$_3$InN (A = Co, Ni) are calculated for spin-up (↑) and spin-down (↓) using high-symmetry *k*-points along the path *X−R−M−G−R* in the first Brillouin zone. The results are displayed in Figure 4(a)−(c). From Figure 4, it is seen that the dispersion curves for up and down spins are different for Co$_3$InN. Two bands for up and two bands for down spin cross the E_F which is shown in Figures 4(a) and 4(b). On the contrary, the dispersion curves for both spins are the same for Ni$_3$InN. Two bands cross the E_F, as seen in Figure 4(c). The dispersion curve for down spin is not shown due to the spin-symmetric nature of Ni$_3$InN. Both Co$_3$InN and Ni$_3$InN exhibit metallic nature, as the conduction and valence bands notably overlap at the Fermi level.

To explore the origin of metallic and magnetic nature, the spin-polarized total density of states (DOS) and orbital-resolved partial DOS (pDOS) are calculated for A$_3$InN. The spin-dependent DOS and pDOS of Co$_3$InN are shown in Figure 5. It is clearly seen that the DOS at the Fermi level is nonzero for both spin channels [Figure 5(a)], revealing the metallic nature of Co$_3$InN with zero energy gap. The observed DOS values are found at 1.176 states/eV and −2.893 states/eV at E_F for the spin-up and spin-down channel, respectively. Thus, the DOS of Co$_3$InN is contributed by both spins but significantly ∼2.5 times higher for the spin-down channel. The contribution of individual atoms in Co$_3$InN that occupied the electronic states per unit energy is determined by the pDOS shown in Figure 5(b)−(d).

It is seen that the valence band of Co$_3$InN is roughly separated into three sub-bands, ranging from (−9.1 to −5) eV, (−5 to −0.5) eV, and (−0.5 to E_F) eV, showing some sharp peaks. These peaks arise due to the hybridization of different electronic states. The lower energy band (−9.1 to −5) eV is contributed by Co-3d, Co-3p, In-5s, In-5p, and N-2p orbitals, whereas the rest of the band is donated by Co-3d, In-5p, and N-2p orbitals. The electrons in the Co-3d orbital contribute strongly in the conduction mechanism of the Co$_3$InN phase for both spin channels. However, the contribution of Co-3p, Co-4s, In-5s, In-5p, and N-2p orbitals is minor. In addition, the DOS and pDOS peaks are seen to be blue-shifted for the spin-down channel, which indicates the presence of strong spin−orbit coupling (SOC) in Co$_3$InN.

The spin-dependent DOS of Ni$_3$InN is shown in Figure 6(a)−(d). The nonzero values of DOS [Figure 6(a)] for both spin channels indicate the metallic nature of Ni$_3$InN. It is notable that the DOS and pDOS patterns of Ni$_3$InN are identical for up and down channels in contrast to the case of Co$_3$InN.
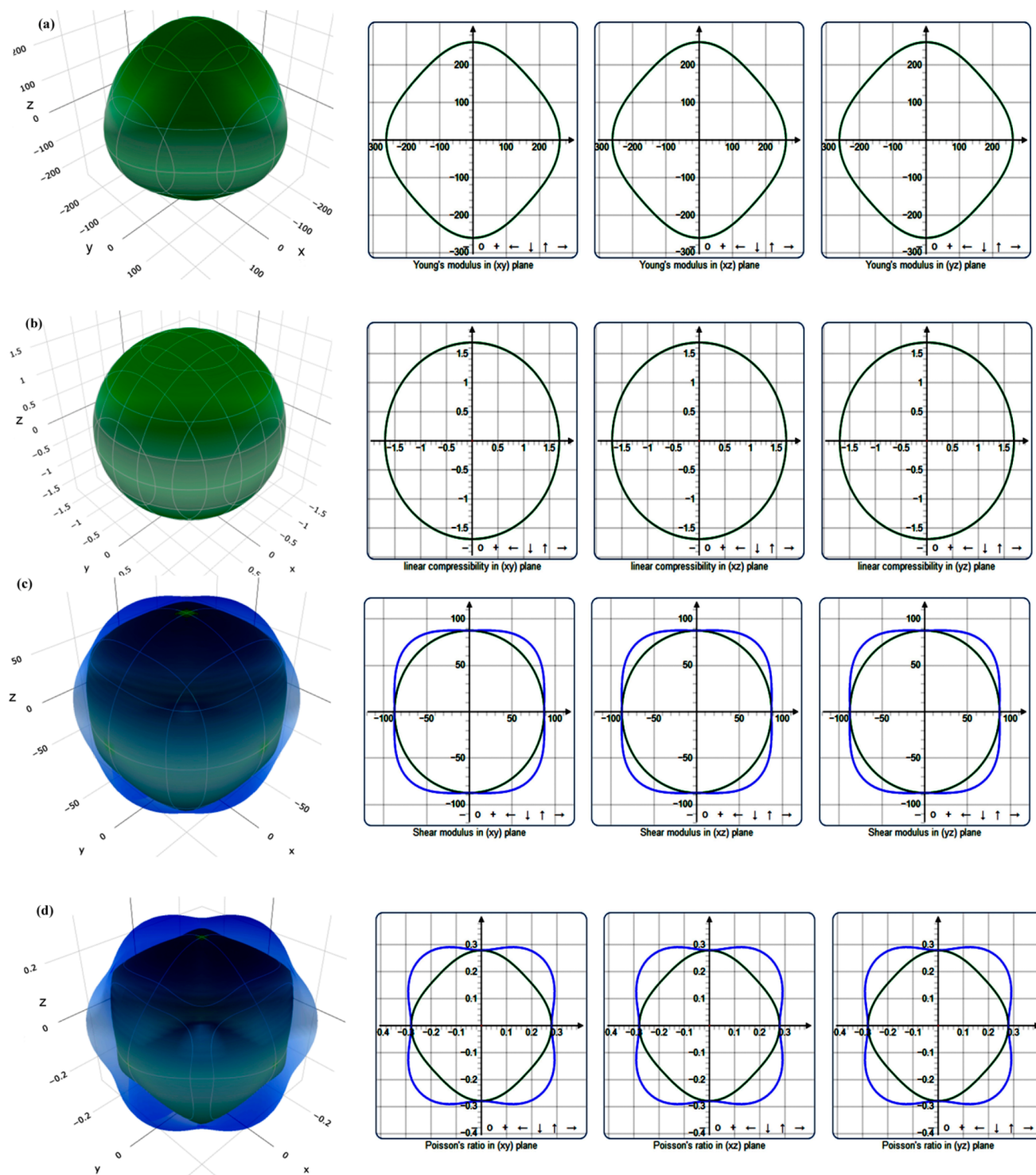
Figure 2. Three- and two-dimensional contour diagrams of (a) Young's modulus (Y), (b) linear compressibility (β), (c) shear modulus (G), and (d) Poisson's (ν) ratio for the Co$_3$InN antiperovskite.

The calculated value of the DOS at the Fermi level is 1.04 states/eV for both spins in Ni$_3$InN. The DOS of Ni$_3$InN is mainly contributed by Ni-3d orbitals, whereas the Ni-3p, In-5s, In-5p, and N-2p orbitals contribute faintly as seen from Figure 6(b)−(d). The valence band of Ni$_3$InN is roughly separated into three sub-bands as Co$_3$InN. The lower (−9.1 to −4.80) eV, middle (−4.80 to −0.792) eV, and top sub-bands that cross E_F result from the hybridization of Ni-3d, Ni-3p, In-5s, and N-2p

orbitals, Ni-3d, Ni-3p, In-5p, and N-2p orbitals, and Ni-3d, Ni-3p, In-5s, In-5p, and N-2p orbitals, respectively. From the pDOS [Figures 5(c) and 6(c)], it is clearly seen that the contribution of an In atom is feeble at E_F, which indicates the bare minimum involvement of the In atom in metal-like conductions of both Co$_3$InN and Ni$_3$InN.

3.4. Magnetic Properties and Molecular Orbital Analysis. The magnetic moments for total and individual
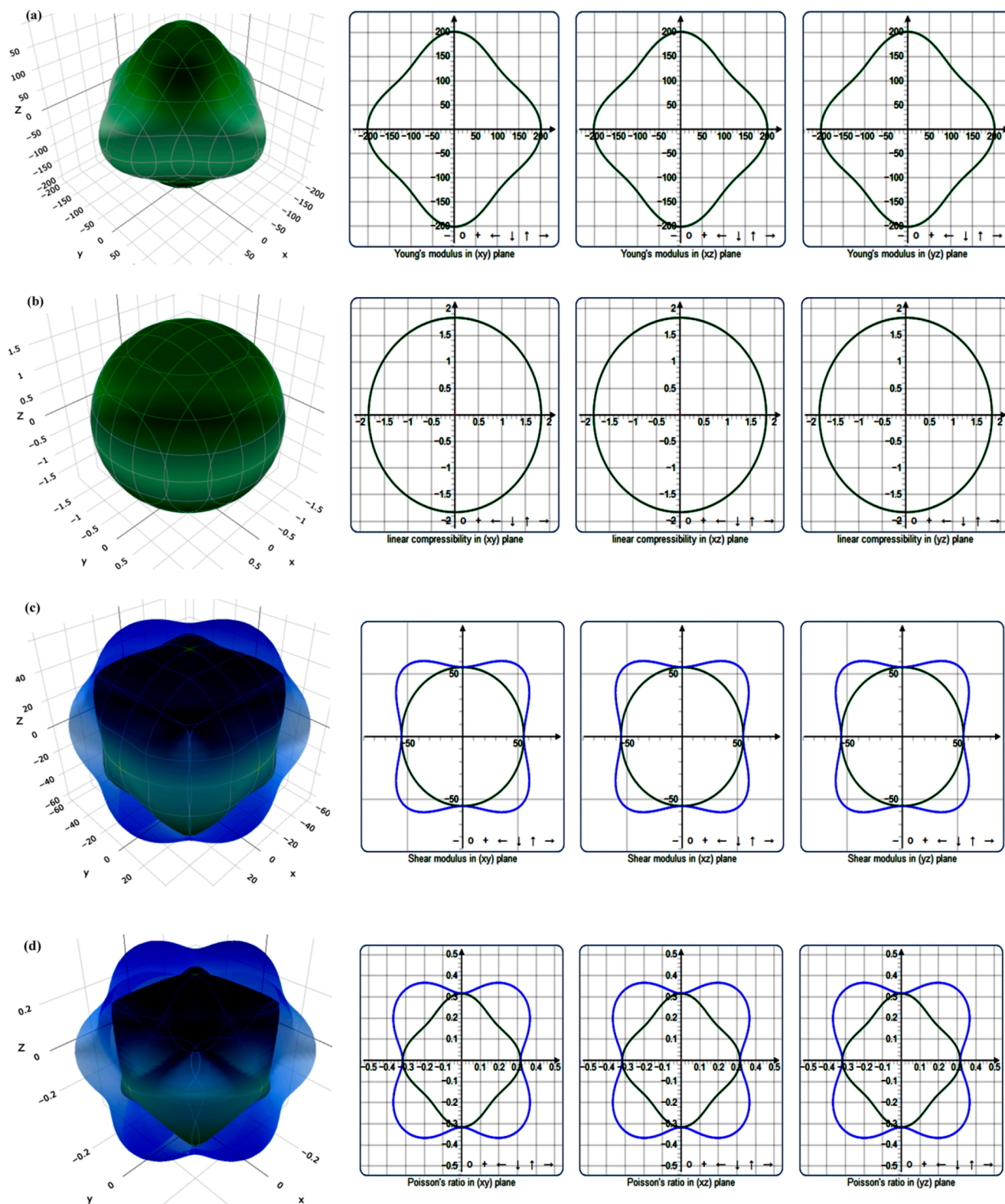
Figure 3. Three and two-dimensional contour diagrams of (a) Young's modulus (Y), (b) linear compressibility (β), (c) shear modulus (G), and (d) Poisson's (ν) ratio for Ni$_3$InN antiperovskite.

atoms are calculated from the integrated DOS at the Fermi level. The magnetic moment in Co$_3$InN may arise due to shifts of the pDOS for spin-up and -down channels. The induced total magnetic moment of Co$_3$InN is 2.735 μ_B/cell, which is contributed by Co, N, and In atoms. The local magnetic

moment is calculated as 0.9163 μ_B, 0.0919 μ_B, and −0.1651 μ_B for Co, N, and In atoms, respectively. On the contrary, the total magnetic moment for Ni$_3$InN is calculated as 0.526×10^{-8} μ_B/cell, which is negligible. It is noteworthy that we have also considered the magnetic unit cell with both ferromagnetic and

Table 4. Minimum and Maximum Limit of Y, β, G, and ν for A$_3$InN (A = Co, Ni)^a

compound	Young's modulus (GPa)		linear compressibility (TPa^{-1})		shear modulus (GPa)		Poisson's ratio		ref
	Y_{max}	Y_{min}	β_{max}	β_{min}	G_{max}	G_{min}	ν_{max}	ν_{min}	
Co$_3$InN	228.79	260.99	1.6893	1.6893	87.543	101.99	0.25286	0.34833	this work
Ni$_3$InN	151.05	200.93	1.8309	1.8309	55.462	76.338	0.25331	0.45183	this work
Ti$_3$TlN	91.04	140.09			32.5	52	0.19	0.54	8
Ni$_3$SnN	114.17	178.44			41	67	0.23	0.53	8
Co$_3$AlC	229.37	401.31			86	166	0.13	0.49	8
Ti$_3$AlC		140			83		0.25		43
Ni$_3$MgC		151			58		0.3		45

^{a}The results of other antiperovskite compounds are listed for comparison.

Table 5. Anisotropy Parameters and Extrema of Poisson's Ratio for A$_3$InN (A = Co, Ni)^a

compound	A_Z	A_G	A_U	A_L	$\nu(110, 001)$	$\nu(110, 1\bar{1}0)$	ref
Co$_3$InN	0.85	0.003	0.00	0.00	0.250	0.352	this work
Ni$_3$InN	0.72	0.129	0.161	0.071	0.247	0.456	this work
Ti$_3$AlC		0.015	0.154				51
Fe$_3$AlC		0.093	1.032				51
Sm$_3$AlC		0.375	6.00				51

^{a}The results of other antiperovskite compounds are listed for comparison.
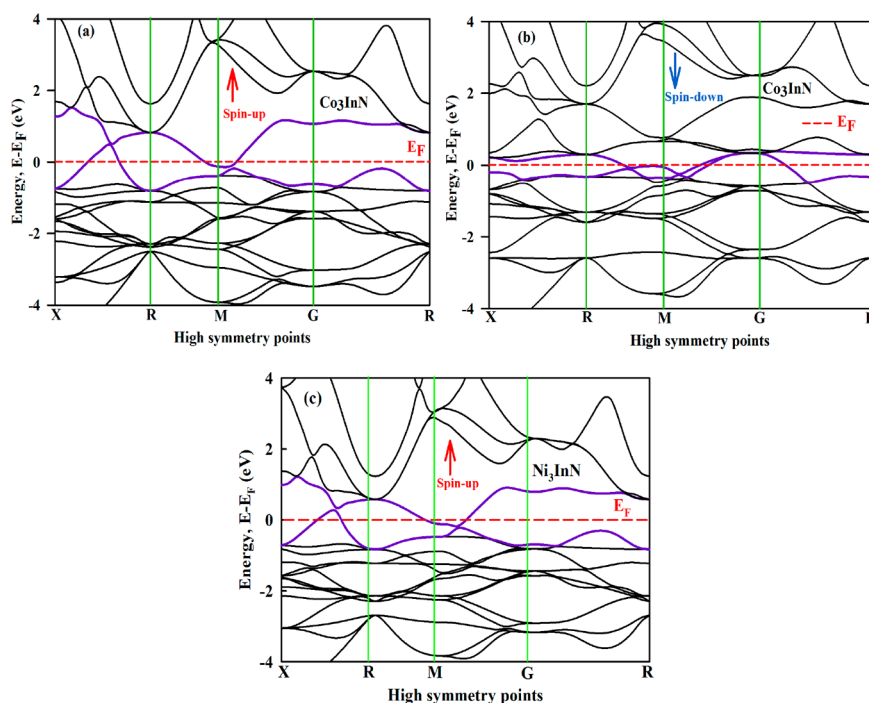

Figure 4. Electronic band structures with (a) spin-up and (b) spin-down channels for Co$_3$InN and (c) the band structure for only the spin-up channel for Ni$_3$InN ternary antiperovskites. The pattern of the band structure of Ni$_3$InN for the down-spin channel is identical with that for the spin-up channel and is not shown here.

antiferromagnetic ordering of Co(Ni) atoms to find out the nature of A$_3$InN. Here it should be mentioned that a single unit cell of A$_3$InN (cf. Figure 1) is enough for both ferromagnetic (where all A atoms are in the same spin orientation) and antiferromagnetic settings (A atoms in alternate layers are with opposite spin orientations) and considered as a magnetic unit cell. Our calculations suggest that Co$_3$InN (Ni$_3$InN) is ferromagnetic (nonmagnetic) in nature.

In order to further understand the magnetic nature and the contribution of s, p, and d orbitals fully in the band structure of

A$_3$InN, we pictured the orbital hybridization among different atoms based on orbital-projected band diagrams. Comparing Figures 5(b) and 6(b), it is clear that for empty states in the pDOS Co-3d states have a significant contribution only for the down-spin channel but a nominal contribution for the up spin of Co-3d and for both spin channels of Ni-3d. These findings of pDOS characteristics are similar to an earlier study.[3] For the next part, we consider only the down-spin channel.

Orbital-projected band diagrams along $\Gamma-X-R-M-\Gamma-R$ directions for Co$_3$InN and Ni$_3$InN are evaluated using the
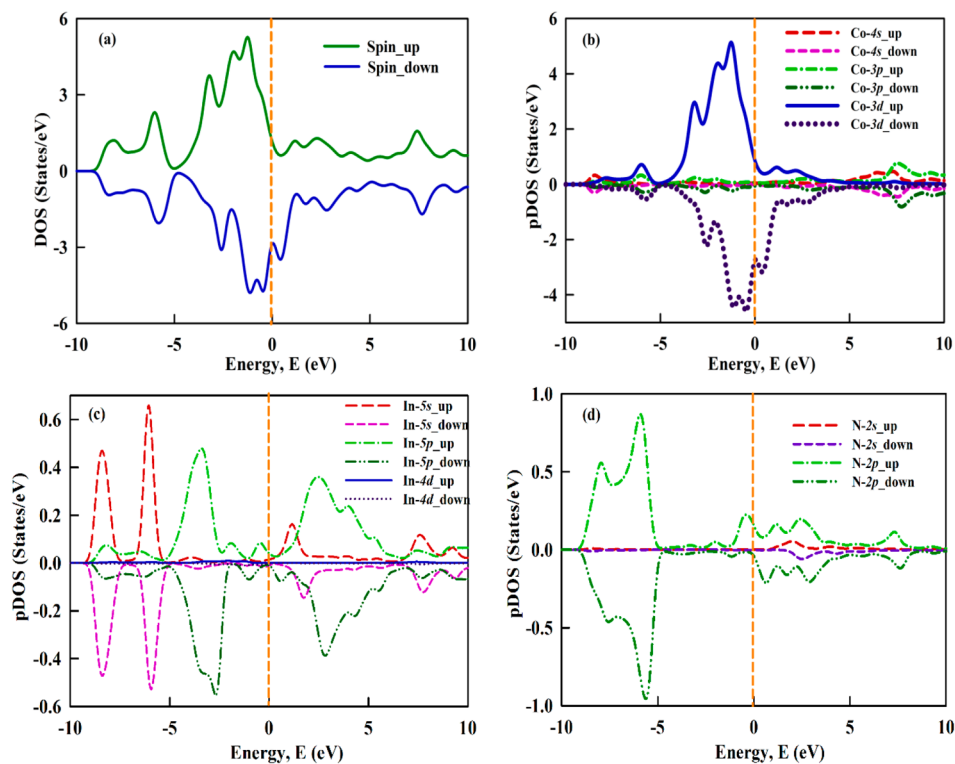
Figure 5. (a) Total density of states (DOS) and (b−d) partial density of states (pDOS) of the Co_3InN antiperovskite.
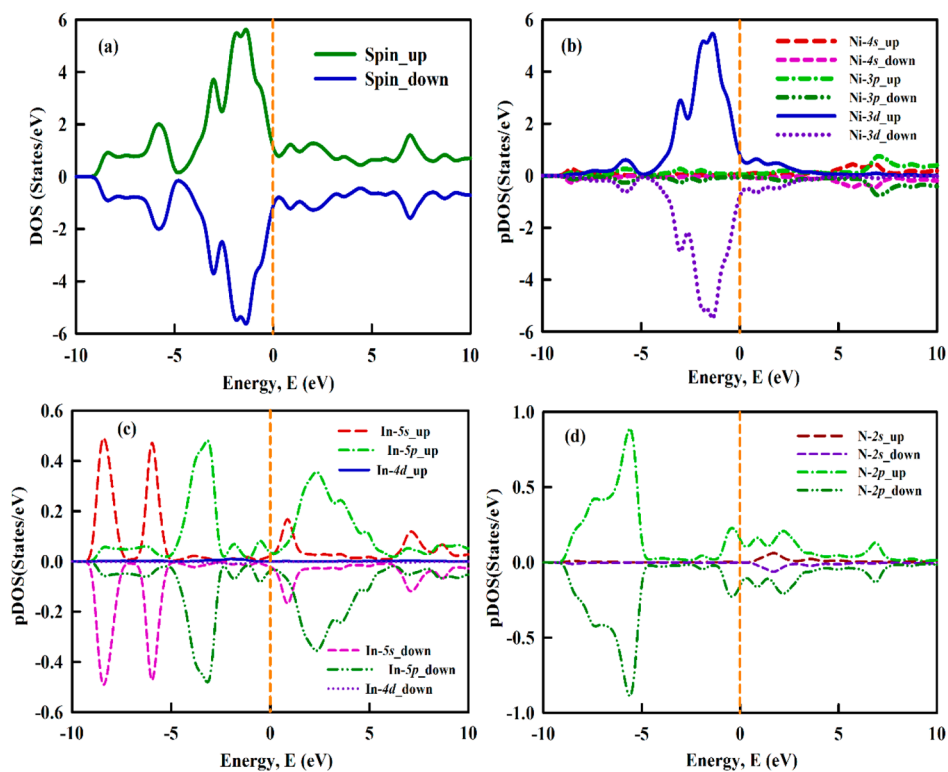

Figure 6. (a) Total density of state (DOS) and (b−d) partial density of states (pDOS) of Ni_3InN antiperovskite.

Quantum ESPRESSO[36] code and presented in fat band representation in Figures 7 and 8, respectively. In these figures, the vertical width of the belts (dispersion lines) represents spectral weights of (a) Co/Ni-e_g (d_{z^2}, $d_{x^2-y^2}$), (b) Co/Ni-t_{2g} (d_{xz}, d_{yz}, d_{xy}), (c) In-t_{1u} (p_x, p_y, p_z), (d) N-t_{1u} (p_x, p_y, p_z), and (e) In

a_{1g}(s) orbitals, respectively. For better clarity, orbital-projected bands are not superimposed on normal band dispersion curves. Figures 7 and 8 represent normal band dispersion curves where the orbital degeneracy at different energy levels is identified by red color orbital symbols on the vertical line along the high-
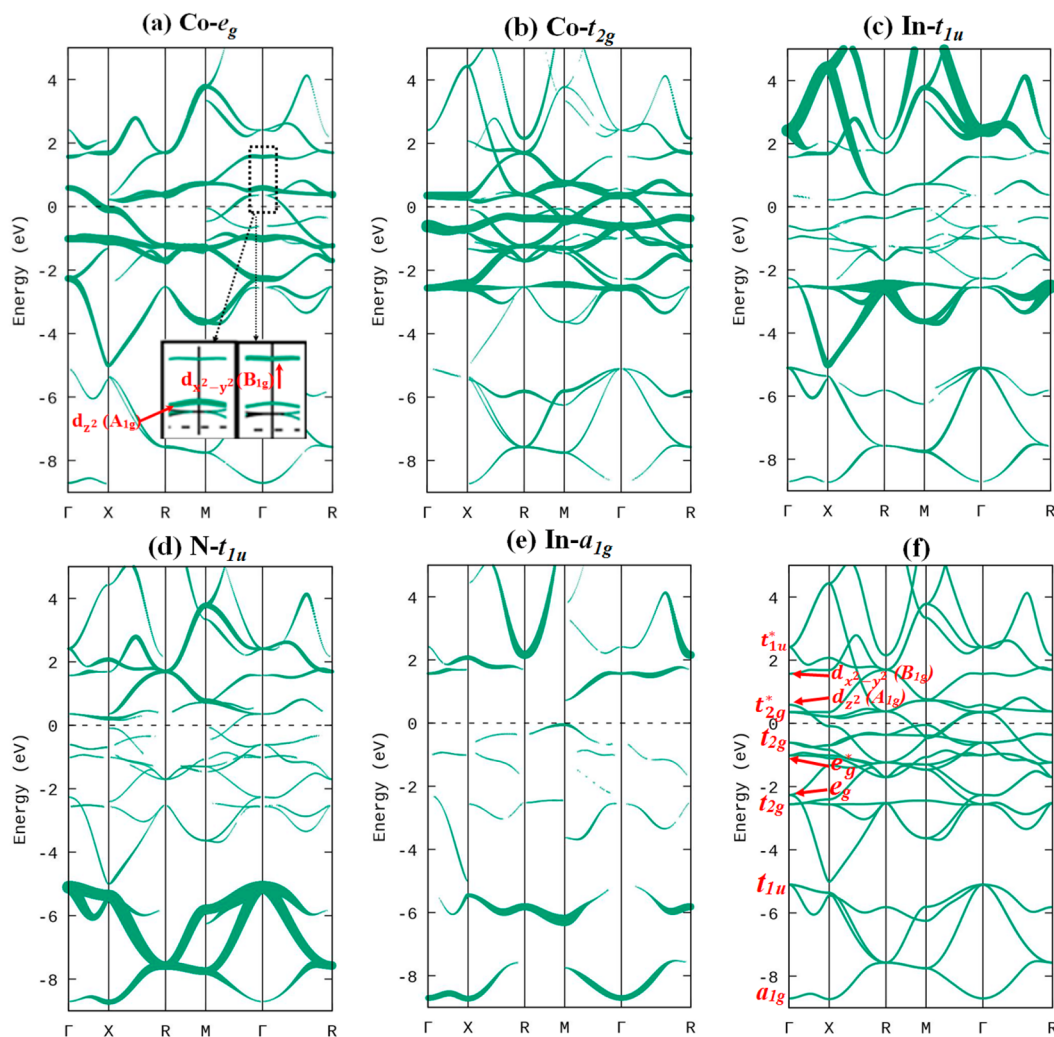
Figure 7. Orbital projected band structure of Co_3InN for spin-down channels in a fat band representation along $\Gamma-X-R-M-\Gamma-R$ directions. Vertical width of the belts (dispersion curves) represents spectral weights of (a) $Co-e_g$, (b) $Co-t_{2g}$, (c) $In-t_{1u}$, (d) $N-t_{1u}$, and (e) $In-a_{1g}$ orbitals, respectively. For better clarity, orbital projected bands are not superimposed on normal band dispersion curves. (f) Represents normal band dispersion curves where the orbital degeneracy at different energy levels is identified by red color symbols on the vertical line along the high-symmetry point Γ. The Fermi energy is set to zero and shown by a dashed black line. The inset of (a) is for two separate calculations considering $Co-d_{x^2-y^2}$ and $Co-d_{z^2}$ orbitals, respectively, and the vertical width of the belt confirms that the 2-fold degeneracy of e_g is broken, and it splits in two orbitals $d_{x^2-y^2}$ (B_{1g}) and d_{z^2} (A_{1g}), respectively, where the energy of $d_{x^2-y^2}$ is greater than that of d_{z^2}.

symmetry point Γ. The Fermi energy is set to zero and shown by a dashed black line. The inset of Figure 7(a) is for two separate calculations considering $Co-d_{x^2-y^2}$ and $Co-d_{z^2}$ orbitals, respectively, and the vertical width of the belts confirms that the 2-fold degeneracy of e_g is broken, and it splits in two orbitals $d_{x^2-y^2}$ (B_{1g}) and d_{z^2} (A_{1g}), respectively, where the energy of $d_{x^2-y^2}$ is greater than that of d_{z^2}. The findings are similar for Ni_3InN where 2-fold degeneracy of e_g is also broken with $d_{x^2-y^2} > d_{z^2}$ and not shown in the inset of Figure 8(a).

From Figures 7 and 8, it is seen that the band structure of Co_3InN (Ni_3InN) is projected into Co (Ni)-e_g (d_{z^2}, $d_{x^2-y^2}$) and t_{2g} (d_{xz}, d_{yz}, d_{xy}), $In/N-t_{1u}$ (p_x, p_y, p_z), and a_{1g} (s) orbitals. The Eigen states at the Γ point in the Brillouin zone are considered to explain the orbital hybridization process. Figure 9(b) and 9(c) represents the crystal field splitting and the possible hybridization between d-orbitals of $Co-Co/Ni-Ni$ and s- and p-orbitals of In/N atoms. These hybridizations arise due to interactions of the bonding and the antibonding states of the orbitals.

Antiperovskite A_3InN (A = Co, Ni) compounds with Hermann–Mauguin notation $m\bar{3}m$ belong to octahedral (O_h) symmetry.[1] Within Co_3InN (Ni_3InN), N and In atoms are coordinated by 6 and 12 Co (Ni) atoms, respectively, forming a Co_6N (Ni_6N) octahedron and $Co_{12}In$ ($Ni_{12}In$) cuboctahedron, respectively.[1] In A_3InN (A = Co, Ni), In and N atoms occupy Wyckoff positions a (0, 0, 0) and b (1/2, 1/2, 1/2) with the site symmetry of O_h, and 3 A atoms occupy Wyckoff positions c (0, 1/2, 1/2) with the site symmetry D_{4h}, respectively.[52]

Here we used e_g (d_{z^2}, $d_{x^2-y^2}$), t_{2g} (d_{xz}, d_{yz}, d_{xy}), t_{1u} (p_x, p_y, p_z), and a_{1g} (s) symbols of O_h symmetry for orbitals shown in the first bracket. We also used A_{1g} (d_{z^2}), B_{1g} ($d_{x^2-y^2}$), B_{2g} (d_{xy}), and E_g (d_{xz}, d_{yz}) symbols of D_{4h} symmetry for orbitals shown in the first bracket in the molecular orbital diagram for considering A–A hybridization between 3d orbitals of two A atoms with local site symmetry D_{4h} [cf. Figure 9(a)].

Based on the orbital-projected band diagrams (Figures 7 and 8), we predicted a possible hybridization scheme which is explained below. Figure 9(b) and 9(c) is molecular orbital
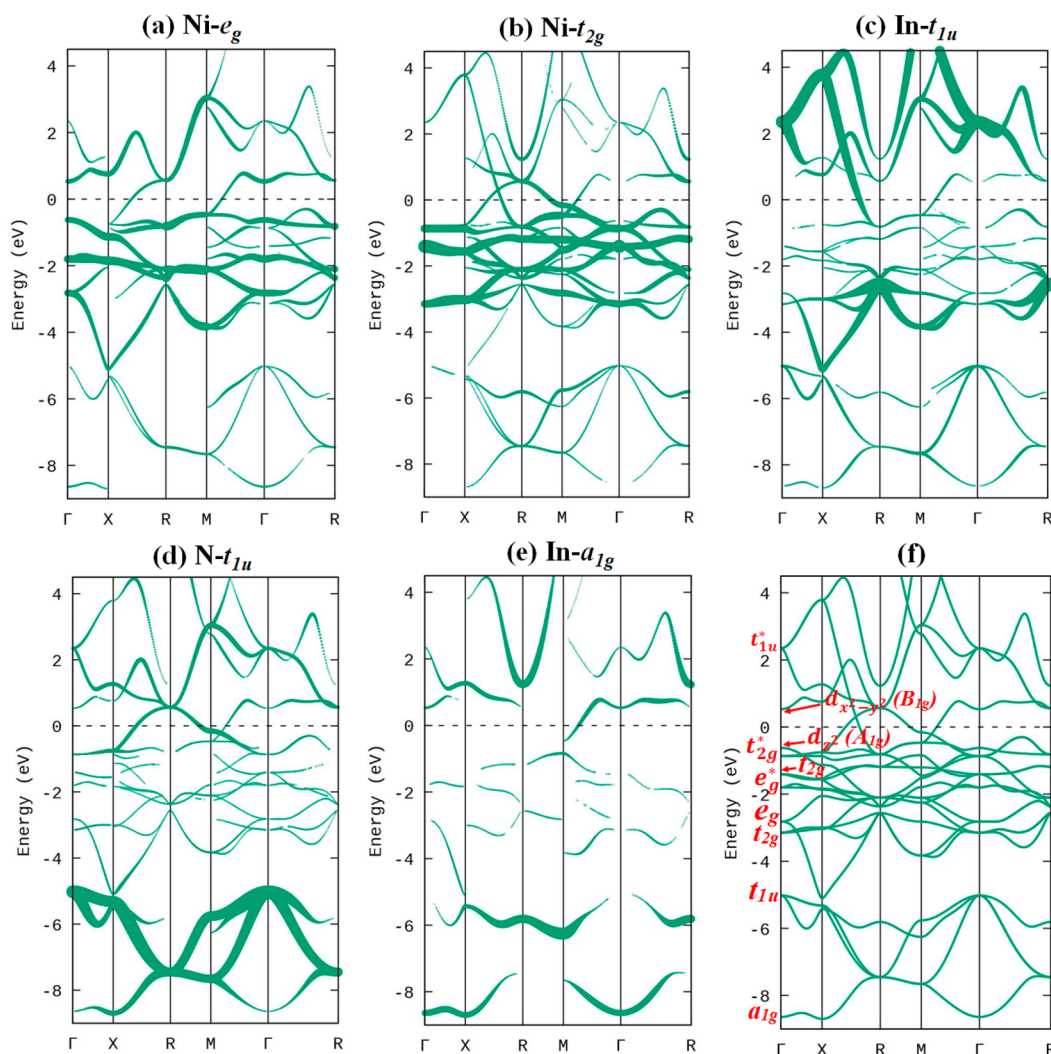
Figure 8. Orbital-projected band structure of Ni$_3$InN for the spin-down channel in fat band representation along $\Gamma-X-R-M-\Gamma-R$ directions. Vertical width of the belts (dispersion curves) represents spectral weights of (a) Ni-e_g, (b) Ni-t_{2g}, (c) In-t_{1u}, (d) N-t_{1u}, and (e) In-a_{1g} orbitals, respectively. For better clarity, orbital-projected bands are not superimposed on normal band dispersion curves. (f) Represents normal band dispersion curves where the orbital degeneracy at different energy levels is identified by red color symbols on the vertical line along high symmetry point Γ. The Fermi energy is set to zero and shown by a dashed black line. The 2-fold degeneracy of e_g is broken, and it splits in two orbitals d$_{x^2-y^2}$ (B_{1g}) and d$_{z^2}$ (A_{1g}), respectively, as marked in (f), confirmed by two separate calculations (not shown here) considering Ni-d$_{x^2-y^2}$ and Ni-d$_{z^2}$ orbitals, respectively (for details see text).

diagrams between spin-down orbitals sitting at different sites in the case of the Co$_3$InN and Ni$_3$InN antiperovskites, respectively. Here we used a similar approach as used in earlier studies to construct the MO diagrams of other perovskites with different crystal structures (such as X$_2$YZ).[32,53,54] Here the hybridizations between the two different A (A = Co, Ni) atoms with D_{4h} site symmetry are considered first [cf. Figure 9(a)]; afterward A–A and an N (site symmetry O_h) atoms are hybridized with another A and an In (site symmetry O_h) atoms, respectively. The site-symmetry approach establishes symmetry relations between the localized atomic electron states and crystalline states; then the localized states transform following the overall crystal symmetry.

Here, the hybridization and combination of double-degenerated E_g (d$_{xz}$, d$_{yz}$) and single-degenerated B_{2g} (d$_{xy}$) of A–A and A with symmetry D_{4h} transformed according to O_h symmetry to produce triple-degenerated bonding t_{2g} orbitals and antibonding t_{2g}^* orbitals. On the other hand, the hybridization and combination of two single-degenerated A_{1g} (d$_{z^2}$) and B_{1g}

(d$_{x^2-y^2}$) of A–A and A with symmetry D_{4h} transformed according to O_h symmetry to produce double-degenerated bonding e_g orbitals and antibonding e_g^* orbitals. Due to the unavailability of more sites with D_{4h} symmetry to hybridize the antibonding states of A–A: E_g^* (d$_{xz}$, d$_{yz}$), A_{1g}^* (d$_{z^2}$), B_{2g}^* (d$_{xy}$), and B_{1g}^* (d$_{x^2-y^2}$) remain as nonbonding in the resulting MO orbital diagram [cf. Figures 9(b) and 9(c)]. However, double-degenerated E_g (d$_{xz}$, d$_{yz}$) and single-degenerated B_{2g} (d$_{xy}$) of A–A with symmetry D_{4h} combined and transformed according to O_h symmetry to produce the nonbonding triple-degenerated t_{2g} state. Interestingly, two remaining nonbonding orbitals A_{1g} (d$_{z^2}$) and B_{1g} (d$_{x^2-y^2}$) do not combine to create a double-degenerated nonbonding e_g state.

As a whole for Co$_3$InN, we postulate in addition to bonding (a_{1g}, t_{1u}, t_{2g}, and e_g) and antibonding (e_g^*, t_{2g}^*, and t_{1u}^*) states the hybridizations of Co–Co [Figure 9(a)] and N with another Co, and an In atom also produces one nonbonding 3-fold t_{2g} and one nonbonding e_g state with broken 2-fold degeneracy [cf. Figure
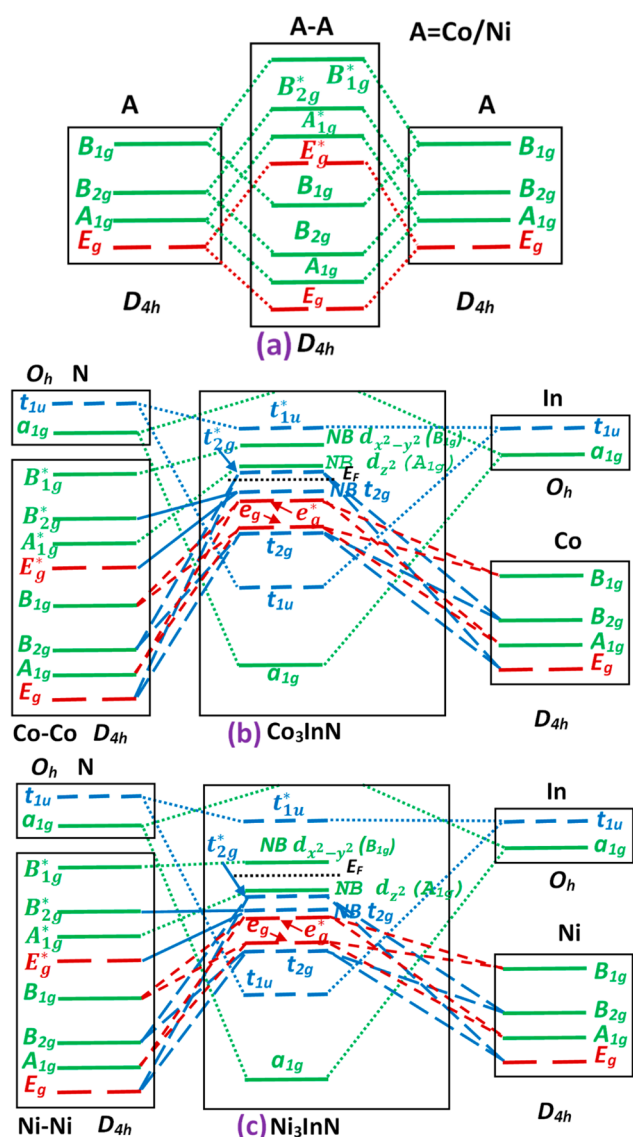
Figure 9. Schematic molecular orbital diagram between spin-down orbitals sitting at different sites in the case of the (b) Co_3InN and (c) Ni_3InN antiperovskites. First, the hybridization between the two different A (A = Co/Ni) atoms with D_{4h} site symmetry are considered (a). Afterward A−A and an N atom (with O_h site symmetry) are hybridized with another A and an In (with O_h site symmetry) atom. The Fermi energy is shown by a dashed black line. The 1-, 2-, and 3-fold degenerate states are shown by green, red, and blue colors, respectively. Here NB refers to the nonbonding and (*) antibonding state. The 2-fold degenerate state e_g splits into two NB orbitals $d_{x^2-y^2}$ (B_{1g}) and d_{z^2} (A_{1g}), respectively.

9(b)]. In the molecular orbital diagram, it is also clear that the e_g state splits in two orbitals $d_{x^2-y^2}$ (B_{1g}) and d_{z^2} (A_{1g}), respectively, where $d_{x^2-y^2} > d_{z^2}$, as confirmed by separate calculations considering Co-$d_{x^2-y^2}$ and Co-d_{z^2} orbitals separately, compared with the inset of Figure 7(a). Such splitting might be due to local Jahn−Teller distortion, which we believe is a local z-out distortion of O_h complexes which results $d_{x^2-y^2} > d_{z^2}$.[55] In the molecular orbital diagram of Co_3InN, one antibonding t_{2g}^* state is above E_F, followed by nonbonding d_{z^2} and $d_{x^2-y^2}$ states toward higher energy.

The p orbitals of N and In atoms hybridize and form bonding and antibonding states of t_{1u} orbitals, whereas s orbitals hybridize and form bonding and antibonding a_{1g} orbitals. The antibonding state a_{1g}^* is above the considered energy window and does not appear in this diagram. The triple-degenerated nonbonding Co (t_{2g}) state dominates the highest orbital state in the valence band of Co_3InN.

The formation of a molecular orbital energy diagram for Ni_3InN [Figure 9(c)] is similar to Co_3InN with respect to hybridization and orbital sequencing. However, the orbital positions with respect to E_F and separations [compare Figure 9(b) with Figure 9(c)] between them are different. An earlier DFT study postulated that Ni-based ternary nitrides with cubic antiperovskite structure are nonmagnetic due to hybridization between Ni-3d and N-2p states.[3] Our results presented above do not support such a hybridization scheme. Interestingly, in the molecular orbital diagram for Ni_3InN [Figure 9(c)], E_F lies between two nonbonding d_{z^2} and $d_{x^2-y^2}$ states. These two nonbonding states in the immediate vicinity of E_F might be the reason for almost zero magnetism in Ni_3InN.

3.5. Mulliken Populations Analysis. The nature of chemical bonding via the charge transfer mechanism in a compound can be predicted using the Mulliken atomic population analysis. The Mulliken atomic and bond overlap populations of A_3InN are tabulated in Table 6.

From Table 6, it is seen that N atoms contain negative Mulliken charge, while it is positive for A (Co, Ni) and In atoms. Hence, charges transferred from A/In to N atoms, which indicates the presence of ionic bonding in A_3InN. The ionic nature of A_3InN can be restricted by the electronegativities of the atomic species. The distribution of carrier density in different bonds and a quantitative measure of bonding and antibonding strengths in A_3InN are described by the Mulliken bond overlap population (BOP) analysis. In general, the positive and negative BOP stands for the bonding and antibonding nature of atoms, respectively. The high and low values of BOP point out the increase of covalent and ionic bond nature, respectively, between two atoms.[56] In this study, the N−A bonds possess a higher degree of covalency with bonding nature. The

Table 6. Mulliken Atomic and Bond Overlap Populations of A_3InN (A = Co, Ni)[a]

| phase | atoms | Mulliken atomic population | | | | Mulliken bond overlap population | | | | |
		s	p	d	total	charge (e)	bond	n^μ	P^μ	d^μ (Å)
Co_3InN	N	1.68	4.02	0.0	5.71	−0.71	N−Co	03	2.01	1.94
	Co	1.29	2.01	23.43	26.73	0.27	Co−In	03	0.21	2.74
	In	0.56	2.02	9.97	12.55	0.45	Co−Co	03	−1.17	2.74
Ni_3InN	N	1.65	4.00	0.0	5.65	−0.65	N−Ni	03	1.92	1.95
	Ni	1.20	2.16	26.43	29.79	0.21	Ni−In	03	−0.03	2.76
	In	0.65	1.93	9.97	12.56	0.44	Ni−Ni	03	−0.57	2.76

[a]n^μ, P^μ, and d^μ denote the bond number, bond overlap population, and bond length, respectively.
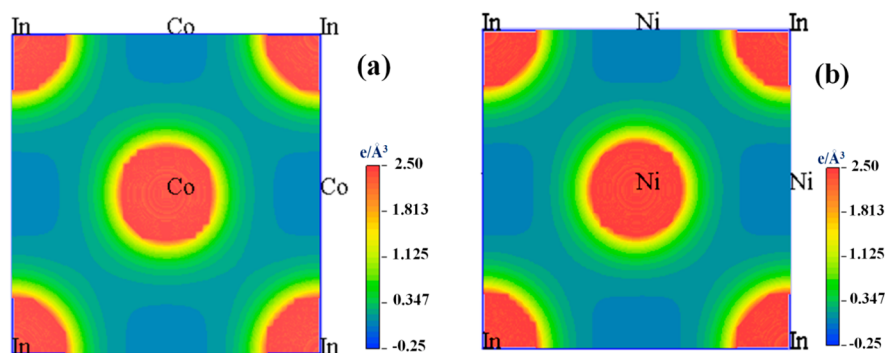
Figure 10. Electronic charge density mappings of (a) Co$_3$InN and (b) Ni$_3$InN ternary antiperovskites on the (001) crystallographic plane.
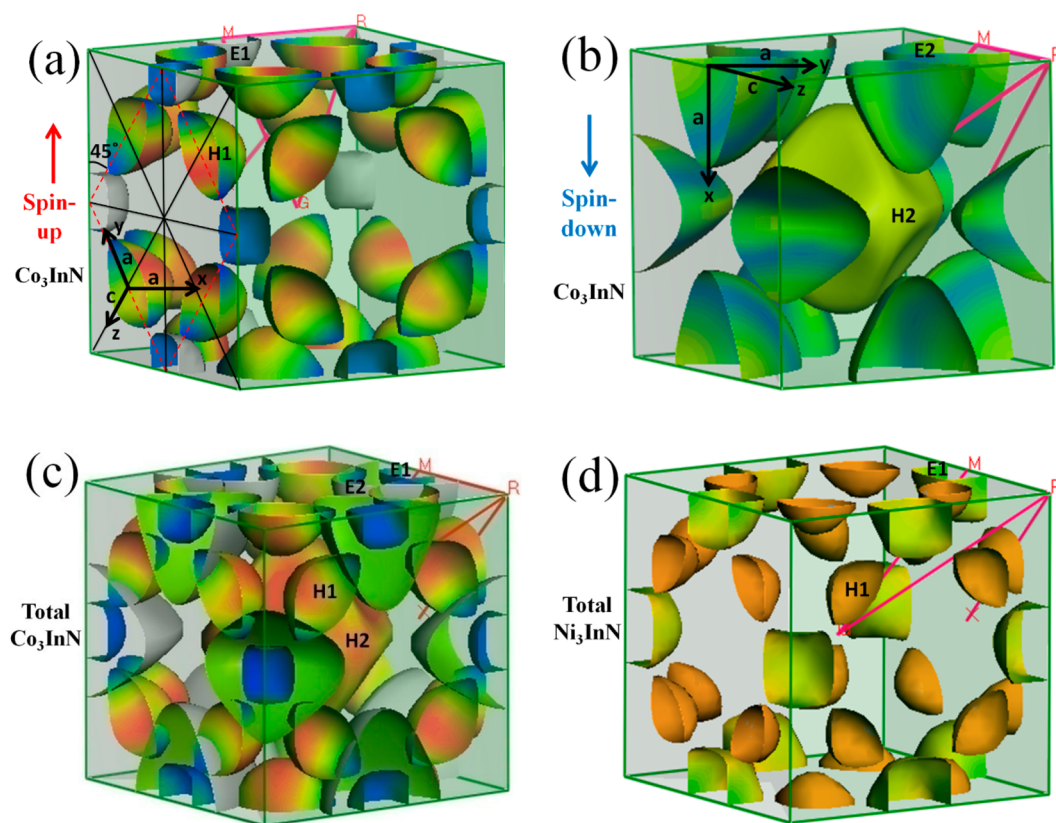

Figure 11. Fermi surface topologies for (a) spin-up, (b) spin-down, (c) total channel of Co$_3$InN, and (d) total channel of Ni$_3$InN.

Co−In bond is also covalent, whereas A−A bonds show ionic nature.

3.6. Charge Density Distribution Mapping and the Fermi Surface. The bonding nature of A$_3$InN (A = Co, Ni) is investigated by the charge density difference of unlike atomic sites for further insights. The charge density mapping of A$_3$InN is shown in Figure 10 on the (001) crystallographic plane. The high and low charge density of electrons is indicated by red and blue colors of the adjacent scale bar, respectively. In general, the greater accumulation of charges (positive value) is favorable for the formation of covalent bonds between two atoms, while the negative value or the lower accretion of charges indicates the formation of ionic binding. The contour maps of electron charge density show higher accumulation of charges in (A, In) than (A, A) atoms, which is consistent with the Mulliken bond population analysis. Moreover, the spherical charge distribu-

tions around A atoms indicate the ionic nature of chemical bonds in A$_3$InN.

The conception of Fermi surface is regarded as the heart for understanding the state of a compound with metallic nature. The dynamical properties of a material largely depend on the position and shape of the Fermi surface with respect to the Brillouin zone (BZ).[57,58] The Fermi surface topology of the ternary nitride perovskite A$_3$InN is evaluated in the equilibrium structure with spin-polarized conditions at zero pressure. It is important to note that the effect of spin channels is absent on the Fermi surface of Ni$_3$InN. This spin-independent nature of the Fermi surface for Ni$_3$InN is also supported by band dispersion study. The Fermi surface topologies for spin-up, spin-down, total channel of Co$_3$InN, and total channel of Ni$_3$InN are shown in Figure 11(a)−(d), respectively, and explained separately below.
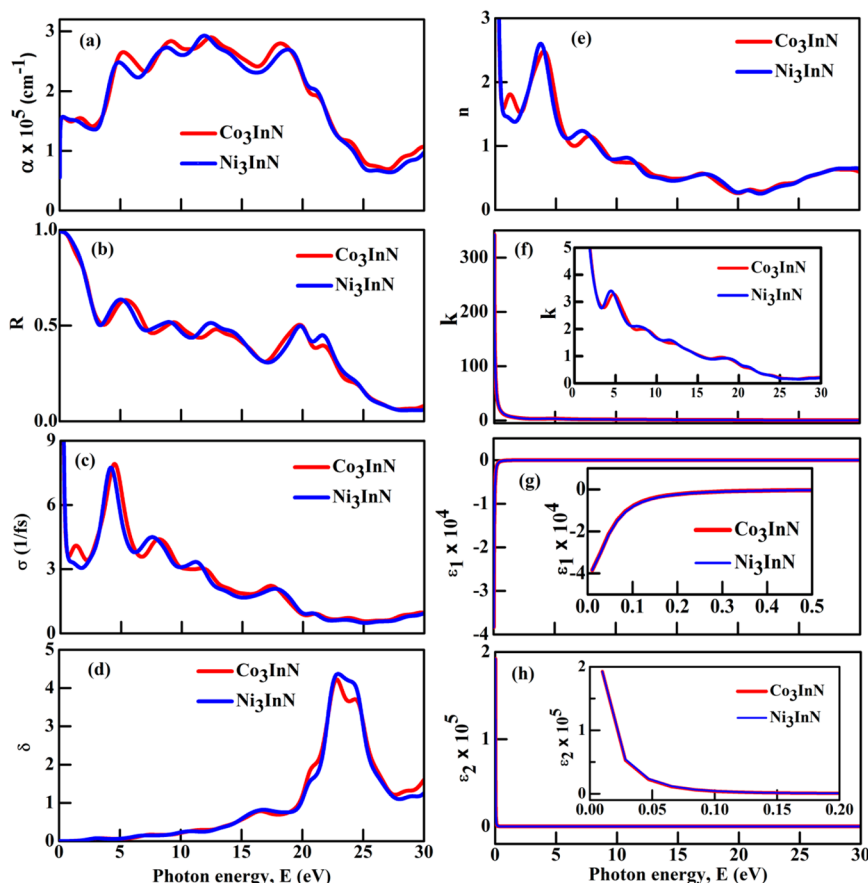
Figure 12. Energy-dependent different nonlinear optical constants along the [100] electric field polarization: (a) absorption coefficient, (b) reflectivity, (c) photoconductivity, (d) loss function, (e) refractive index, (f) extinction coefficient, (g) real part of the dielectric function, and (h) imaginary part of the dielectric function of Co_3InN and Ni_3InN ternary antiperovskites.

Co_3InN with spin-up channel: (1) Half of an oblate-spheroid-shaped open surface between high-symmetry points X, and R [marked by H1 in Figure 11(a)] within the BZ is a hole pocket. A total of 24 such hole pockets are visible at the 6 zone faces. The conventional equation of the oblate spheroid is written as

$$\frac{x^2 + y^2}{a^2} + \frac{z^2}{c^2} = 1$$

where x-, y-, and z-axes intercepts are a, a, and c, respectively, and $a > c$. One hole pocket at the right face of the BZ cube is marked to show the x, y, z directions and their a, a, c intercepts. From Figure 11(a), it is evident that the z-direction is considered along the high-symmetry direction X−R. The ratio a:c is calculated as ~3.25:2 ($3.25c = 2a$). The center of the hole pocket is situated exactly at the middle of the two high-symmetry points X and R. The open surface of a hole pocket that cuts the BZ face creates approximately an elliptical shape with the major axis along the y-direction. The elongated 4 of such a major axis on a single BZ face forms a perfect square which is 45° rotated [shown by dotted line, Figure 11(a)] and inscribed within the square of the BZ face. Here it should be mentioned that these hole pockets are not exactly ideal oblate-spheroid-shaped. (2) In addition, at the zone edges, the open surfaces centered at M seen within the BZ are electron pockets [marked by E1 in Figure 11(a)]. They enclose approximately rectangular areas at the adjacent sides of zone faces. It seems if two such surfaces are attached, it will create a dome shape with an approximately square base. A total of 12 such electron pockets are visible in Figure 11(a). Co_3InN

with spin-down channel: (3) Closed surface around the G (gamma) point which very nearly resembles an octahedron with curved edges as observed in Figure 11(b), marked by H2 as a hole pocket. (4) In addition, one fourth of an oblate-spheroid-shaped ($a > c$) open surface centered at M observed at the BZ edge is an electron pocket, marked by E2 in Figure 11(b). The open surfaces of an electron pocket that cuts the adjacent sides of zone faces create half (cut along the minor axis) of an elliptical shape (with equal size, at both sides) with the major axis along a high-symmetry MX direction. One electron pocket at the left-upper edge of BZ is marked to show the x, y, z directions and their a, a, c intercepts of an oblate spheroid. Here, the ratio a/c is calculated as ~3:2 ($3c = 2a$). A total of 12 such electron pockets are visible in Figure 11(b).

Co_3InN with total-spin channel: As both the electron pockets [explained in (2) and (4)] for both up- and down-spin channels are centered at same point M, the Fermi surface nesting is expected as evident in Figure 11(c), where the open surface of an electron pocket (originated from up spin) in turn is nested within another one-fourth portion of a larger oblate-spheroid-shaped open surface of another electron pocket (originated from down spin).

Ni_3InN with total-spin channel: Here a similar explanation holds as Co_3InN with the spin-up channel explained earlier and shown in Figure 11(d). However, here a major difference is that the volume of hole (electron) pockets is smaller (larger) compared to Co_3InN with a spin-up channel. The observations are consistent with the band diagram analysis.

In conclusion, the Fermi surface of A_3InN is composed of multiple electron- and hole-type sheets. The nonspherical shape of Fermi sheets indicates the metallic conductivity of both Co_3InN and Ni_3InN. The multi Fermi sheets of A_3InN are formed due to low dispersion of A-3d, In-5p, and N-2p states, as revealed by pDOS studies. The observed Fermi surface nesting may have an effect on the magnetic order and phonon softening in Co_3InN.[59]

3.7. Optical Properties. The optical properties of A_3InN are calculated as a function of incident photons along the [100] direction. A phenomenological damping constant of 0.05 eV, the free-electron plasma frequency of 10 eV, and Gaussian smearing of 0.5 eV are used for the inclusion of intraband transitions for nonlinear optical constant calculations. The absorption coefficient (α) determines how far the light of a certain wavelength can penetrate into a material before being absorbed. The variation of the absorption coefficient α with photon energy is shown in Figure 12 (a). From this figure, it is clearly seen that the optical absorption starts from zero photon energy, which confirms the absence of optical band gap in A_3InN, complementing the metallic nature obtained in the electronic structure calculations. The absorption coefficient increases sharply in the visible spectrum region (after ~2.5 eV) and displays a high value for a wide energy range (~18 eV). Hence, A_3InN could be used as a promising absorber of electromagnetic radiation for both visible and ultraviolet (UV) regions.

The reflectivity spectra (R) of A_3InN are shown in Figure 12(b). It is seen that A_3InN reflects more that 98% of light at zero photon energy. After that, the reflectivity decreases gradually with increasing photon energy. However, the average reflectivity of A_3InN is >45% in the visible and UV spectral region, which indicates the suitability of A_3InN as a coating material to avoid solar heating.[60]

The optical conductivity (σ) starts at zero photon energy [Figure 12(c)], which reconfirms the metallic nature of A_3InN. The response of σ with photon energy is slightly blue-shifted for Co_3InN compared to Ni_3InN. There is a sharp peak at ~(4.2–4.5) eV which might have arisen due to the interband transitions of charge carriers from occupied to unoccupied orbitals in A_3InN.

The loss function of a material is interconnected with absorption and reflection. It describes the energy loss of charge carrier traveling in a material. The energy loss function (δ) is calculated for A_3InN and shown in Figure 12(d). There is no loss peak observed in the energy range of (0−15) eV due to large absorption of electromagnetic radiation. The highest loss peaks appeared for Co_3InN and Ni_3InN at ~22.80 eV and ~22.94 eV, respectively, which represent the plasma resonance owing to collective charge excitation. The corresponding frequency at which the highest peak of the loss spectrum occurs is called the plasma frequency (ω_p) of the material. Below ω_p, A_3InN is expected to reflect the electric field screening by electrons; otherwise, it is transparent to the incident photon.

The appearance of ω_p in the UV range makes A_3InN reflective in the visible spectral range. The refractive index is a complex parameter, composed of the real and imaginary parts of the complex index of refraction. The real part of the refractive index (n) demonstrates the phase velocity of the electromagnetic wave inside a material. The frequency dependence of the refractive index is shown in Figure 12(e). It is seen that n is higher at low photon energy (<5 eV), which decreases with the increasing photon energy. Both Co_3InN and Ni_3InN display a sharp peak at

~3.78 eV and ~4.06 eV, respectively, due to the intraband transition of electrons.

The imaginary part of the complex index of refraction is known as the extinction coefficient (k), which measures the amount of attenuation of the incident light when traveling through the material. The extinction coefficient of A_3InN is plotted in Figure 12(f). It is seen that A_3InN exhibits a large static value of k, which decreases gradually with higher photon energy. The high static value of k is indicative of metallic conduction in A_3InN.

The macroscopic electronic response of a material is explained by means of the complex dielectric constant as $\varepsilon(\omega) = \varepsilon_1(\omega) + i\varepsilon_2(\omega)$, where, $\varepsilon_1(\omega)$ and $\varepsilon_2(\omega)$ are the real and imaginary part of the dielectric function $\varepsilon(\omega)$, respectively. The response of the real and imaginary part of the dielectric constant with photon energy is plotted in Figure 12(g) and 12(h), respectively. From Figure 12(g), it is seen that A_3InN displays negative values of ε_1 at very low energies, after which ε_1 vanishes. The response of ε_1 at low energy is shown in the inset of Figure 12(g). The negative values of ε_1 at low photon energies signify the Drude-like behavior of A_3InN. On the other hand, A_3InN displays positive values of ε_2 and drops down to zero sharply at very low energies [Figure 12(h)]. The variation of ε_2 at low energies is shown in the inset of Figure 12(h). Both ε_1 and ε_2 disappear at very low photon energy, which signifies the high metallic nature of A_3InN.

4. CONCLUSIONS

In summary, we have investigated the structural, mechanical, spin-dependent electronic and molecular orbital predictions, and magnetic and optical properties of antiperovskites nitrides A_3InN (A = Co, Ni) using the first-principles DFT calculations combined with the spin polarization effect. The calculated values of different elastic moduli show the damage-tolerant, quasi-ductile, easily machinable, and stiff nature of A_3InN. Poisson's ratio, Pugh's ratio, and Cauchy pressure calculations suggest that A_3InN is ductile in nature. The values of elastic anisotropy indices reveal that Co_3InN is more anisotropic in compression, while Ni_3InN is more anisotropic in share. The effect of spin channels is observed in the band structure, DOS, and Fermi surface of Co_3InN only. The Fermi surface of A_3InN is composed of multiple nonspherical electron and hole type sheets, and the observed Fermi surface nesting in Co_3InN might contribute to charge density wave formation and also to enhance the effect of electron−phonon coupling. The induced total magnetic moment of Co_3InN is predicted as 2.735 μ_B/cell, whereas Ni_3InN shows nominal magnetic moments. Molecular orbital diagrams of A_3InN antiperovskites are drawn by analyzing orbital-projected band structures. It is exciting to note that the hybridizations of different energy states are identical for both Co_3InN and Ni_3InN. Therefore, it is expected that it will follow the similar trend for A_3BX compounds.

The bonding nature between atoms of A_3InN is thoroughly explained with the aid of Mulliken atomic populations and charge density calculations. The above-mentioned properties reveal that these compounds display the combined bonding nature like ionic and covalent. The variations of the various optical constants such as real and imaginary parts of the dielectric constant, refractive indices, reflectivity, absorption coefficient, and loss function with the energy of incident radiation show metallic behavior, complementing the outcomes of electronic band structure and DOS calculations. The reflectivity spectra show that A_3InN displays superior reflectivity

in the visible and UV spectral region, which indicates that A_3InN compounds have potential significance to be used as coating materials to evade the solar heat. We hope this work will provide helpful data for the family of antiperovskite materials for further investigation through experiments and theories.

■ AUTHOR INFORMATION

Corresponding Authors

Al Momin Md Tanveer Karim − *Institute for Superconducting and Electronic Materials, AIIM, University of Wollongong, Wollongong, NSW 2500, Australia; Department of Physics, Rajshahi University of Engineering & Technology, Rajshahi 6204, Bangladesh;* ○ orcid.org/0000-0002-2150-6487; Email: tanveerruphy@gmail.com, tanveer@phy.ruet.ac.bd

Md Abdul Kader Zilani − *Department of Physics, Rajshahi University of Engineering & Technology, Rajshahi 6204, Bangladesh;* ○ orcid.org/0000-0002-8996-6420; Email: zilani03@gmail.com

Authors

Md Jubair − *Department of Physics, Rajshahi University of Engineering & Technology, Rajshahi 6204, Bangladesh*

Md Nuruzzaman − *Department of Physics, Rajshahi University of Engineering & Technology, Rajshahi 6204, Bangladesh*

Complete contact information is available at:
https://pubs.acs.org/10.1021/acsomega.1c07039

Notes

The authors declare no competing financial interest.

■ ACKNOWLEDGMENTS

■ REFERENCES

(1) Lehmann, T. S.; Blaschkowski, B.; Niewa, R. Electrochemical Bulk Synthesis of Ternary Nitride Perovskites: Co_3InN and Ni_3InN. *Eur. J. Inorg. Chem.* **2019**, *2019* (13), 1709−1713.

(2) Niewa, R. Metal-Rich Ternary Perovskite Nitrides. *Eur. J. Inorg. Chem.* **2019**, *2019* (32), 3647−3660.

(3) Hou, Z. F. Elastic Properties and Electronic Structures of Antiperovskite-Type $InNCo_3$ and $InNNi_3$. *Solid State Commun.* **2010**, *150* (39−40), 1874−1879.

(4) Cao, W. H.; He, B.; Liao, C. Z.; Yang, L. H.; Zeng, L. M.; Dong, C. Preparation and Properties of Antiperovskite-Type Nitrides: $InNNi_3$ and $InNCo_3$. *J. Solid State Chem.* **2009**, *182* (12), 3353−3357.

(5) Quintela, C. X.; Song, K.; Shao, D. F.; Xie, L.; Nan, T.; Paudel, T. R.; Campbell, N.; Pan, X.; Tybell, T.; Rzchowski, M. S.; Tsymbal, E. Y.; Choi, S. Y.; Eom, C. B. Epitaxial Antiperovskite/Perovskite Heterostructures for Materials Design. *Sci. Adv.* **2020**, *6* (30), 1−8.

(6) Hui, Z.; Zhu, Q.; Liu, C.; Wei, J.; Tang, J.; Ye, L.; Ye, X.; Wang, X.; Zuo, X.; Zhu, X. Synthesis and Physical Properties of Antiperovskite $CuNFe_3$ Thin Films via Solution Processing for Room Temperature Soft-Magnets. *Coatings* **2020**, *10* (3), 270.

(7) Zhang, W.; Liu, Y.; Zhou, Y.; Ching, W.; Li, Q.; Li, W.; Yang, J.; Liu, B. Anti-perovskite carbides and nitrides A_3BX: a new family of damage tolerant ceramics. *J. Mater. Sci. Technol.* **2020**, *40*, 64−71.

(8) Das, K.; Ali, M. A.; Hossain, M. M.; Naqib, S. H.; Islam, A. K. M. A.; Uddin, M. M. Dynamical Stability, Vibrational, and Optical Properties of Anti-Perovskite A_3BX (Ti_3TlN, Ni_3SnN, and Co_3AlC) Phases: A First Principles Study. *AIP Adv.* **2020**, *10* (9), 095226.

(9) Beznosikov, B. V. Predicted Nitrides with an Antiperovskite Structure. *J. Struct. Chem.* **2003**, *44* (5), 885−888.

(10) Takenaka, K.; Takagi, H. Giant Negative Thermal Expansion in Ge-Doped Anti-Perovskite Manganese Nitrides. *Appl. Phys. Lett.* **2005**, *87* (26), 261902.

(11) Burghaus, J.; Kleemann, J.; Dronskowski, R. The Ternary Nitrides $In_xFe_{4-x}N$ ($0 \leq x \leq 0.8$): Synthesis, Magnetic Properties, and Theoretical Considerations. *Zeitschrift fur Anorg. und Allg. Chemie* **2011**, *637* (7−8), 935−939.

(12) Burghaus, J.; Sougrati, M. T.; Möchel, A.; Houben, A.; Hermann, R. P.; Dronskowski, R. Local Ordering and Magnetism in $Ga_{0.9}Fe_{3.1}N$. *J. Solid State Chem.* **2011**, *184* (9), 2315−2321.

(13) Sieberer, M.; Mohn, P.; Redinger, J. Role of Carbon in $AlCNi_3$ and $GaCNi_3$: A Density Functional Theory Study. *Phys. Rev. B - Condens. Matter Mater. Phys.* **2007**, *75* (2), 1−6.

(14) Tong, P.; Sun, Y. P.; Zhu, X. B.; Song, W. H. Strong Spin Fluctuations and Possible Non-Fermi-Liquid Behavior in $AlCNi_3$. *Phys. Rev. B - Condens. Matter Mater. Phys.* **2006**, *74* (22), 1−7.

(15) Tong, P.; Sun, Y. P.; Zhu, X. B.; Song, W. H. Strong Electron-Electron Correlation in the Antiperovskite Compound $GaCNi_3$. *Phys. Rev. B - Condens. Matter Mater. Phys.* **2006**, *73* (24), 1−5.

(16) Wu, S. Q.; Hou, Z. F.; Zhu, Z. Z. Elastic Properties and Electronic Structures of $CdCNi_3$: A Comparative Study with $MgCNi_3$. *Solid State Sci.* **2009**, *11* (1), 251−258.

(17) Rosner, H.; Johannes, M. D.; Pickett, W. E.; Weht, R.; Weht, R.; Tosatti, E.; Tosatti, E. Superconductivity near Ferromagnetism in $MgCNi_3$. *Phys. Rev. Lett.* **2001**, *88* (2), 4.

(18) Wu, S. Q.; Hou, Z. F.; Zhu, Z. Z. Electronic Structure and Magnetic State of $InCNi_3$. *Physica B* **2008**, *403* (23−24), 4232−4235.

(19) Song, B.; Zhou, Y.; Yang, H. M.; Liao, J. H.; Yang, L. M.; Yang, X. B.; Ganz, E. Two-Dimensional Anti-Van't Hoff/Le Bel Array AlB_6 with High Stability, Unique Motif, Triple Dirac Cones, and Super-conductivity. *J. Am. Chem. Soc.* **2019**, *141* (8), 3630−3640.

(20) Yang, L. M.; Bačić, V.; Popov, I. A.; Boldyrev, A. I.; Heine, T.; Frauenheim, T.; Ganz, E. Two-Dimensional Cu_2Si Monolayer with Planar Hexacoordinate Copper and Silicon Bonding. *J. Am. Chem. Soc.* **2015**, *137* (7), 2757−2762.

(21) Yang, L.-M.; Ganz, E.; Chen, Z.; Wang, Z.-X.; Schleyer, P. v. R. Four Decades of the Chemistry of Planar Hypercoordinate Compounds. *Angew. Chem., Int. Ed.* **2015**, *54* (33), 9468−9501.

(22) Yang, L. M.; Popov, I. A.; Boldyrev, A. I.; Heine, T.; Frauenheim, T.; Ganz, E. Post-anti-van\textquotesinglet Hoff-Le Bel motif in atomically thin germanium−copper alloy film. *Phys. Chem. Chem. Phys.* **2015**, *17* (27), 17545−17551.

(23) Yang, L. M.; Popov, I. A.; Frauenheim, T.; Boldyrev, A. I.; Heine, T.; Bačić, V.; Ganz, E. Revealing unusual chemical bonding in planar hyper-coordinate Ni_2Ge and quasi-planar Ni_2Si two-dimensional crystals. *Phys. Chem. Chem. Phys.* **2015**, *17* (39), 26043−26048.

(24) Yang, L. M.; Ganz, E. Adding a new dimension to the chemistry of phosphorus and arsenic. *Phys. Chem. Chem. Phys.* **2016**, *18* (26), 17586−17591.

(25) Yang, L. M.; Frauenheim, T.; Ganz, E. The new dimension of silver. *Phys. Chem. Chem. Phys.* **2015**, *17* (30), 19695−19699.

(26) Yang, L. M.; Dornfeld, M.; Frauenheim, T.; Ganz, E. Glitter in a 2D monolayer. *Phys. Chem. Chem. Phys.* **2015**, *17* (39), 26036−26042.

(27) Uehara, M.; Uehara, A.; Kozawa, K.; Kimishima, Y. New Antiperovskite-Type Superconductor ZnN_yNi_3. *J. Phys. Soc. Jpn.* **2009**, *78* (3), 33702.

(28) He, B.; Dong, C.; Yang, L.; Chen, X.; Ge, L.; Mu, L.; Shi, Y. CuNNi3: A New Nitride Superconductor with Antiperovskite Structure. *Supercond. Sci. Technol.* **2013**, *26* (12), 125015.

(29) Uehara, M.; Uehara, A.; Kozawa, K.; Yamazaki, T.; Kimishima, Y. New antiperovskite superconductor $ZnNNi_3$, and related compounds $CdNNi_3$ and $InNNi_3$. *Physica C* **2010**, *470*, S688−S690.

(30) He, B.; Dong, C.; Yang, L.; Ge, L.; Chen, H. Preparation and physical properties of antiperovskite-type compounds $CdNCo_{3-z}Ni_z$ ($0 \leq z \leq 3$). *J. Solid State Chem.* **2011**, *184* (8), 1939−1945.

(31) Graf, T.; Felser, C.; Parkin, S. S. P. Simple Rules for the Understanding of Heusler Compounds. *Prog. Solid State Chem.* **2011**, *39* (1), 1−50.

(32) Nawa, K.; Miura, Y. Exploring Half-Metallic Co-Based Full Heusler Alloys Using a DFT+: U Method Combined with Linear Response Approach. *RSC Adv.* **2019**, *9* (52), 30462−30478.

(33) Segall, M. D.; Lindan, P. J. D.; Probert, M. J.; Pickard, C. J.; Hasnip, P. J.; Clark, S. J.; Payne, M. C. First-Principles Simulation: Ideas, Illustrations and the CASTEP Code. *J. Phys.: Condens. Matter* **2002**, *14* (11), 2717−2744.

(34) Perdew, J. P.; Burke, K.; Ernzerhof, M. Generalized Gradient Approximation Made Simple. *Phys. Rev. Lett.* **1996**, *77* (18), 3865−3868.

(35) Fischer, T. H.; Almlof, J. General Methods for Geometry and Wave Function Optimization. *J. Phys. Chem.* **1992**, *96* (24), 9768−9774.

(36) Giannozzi, P.; Baroni, S.; Bonini, N.; Calandra, M.; Car, R.; Cavazzoni, C.; Ceresoli, D.; Chiarotti, G. L.; Cococcioni, M.; Dabo, I.; Dal Corso, A.; De Gironcoli, S.; Fabris, S.; Fratesi, G.; Gebauer, R.; Gerstmann, U.; Gougoussis, C.; Kokalj, A.; Lazzeri, M.; Martin-Samos, L.; Marzari, N.; Mauri, F.; Mazzarello, R.; Paolini, S.; Pasquarello, A.; Paulatto, L.; Sbraccia, C.; Scandolo, S.; Sclauzero, G.; Seitsonen, A. P.; Smogunov, A.; Umari, P.; Wentzcovitch, R. M. QUANTUM ESPRESSO: A Modular and Open-Source Software Project for Quantum Simulations of Materials. *J. Phys.: Condens. Matter* **2009**, *21* (39), 395502.

(37) Born, M. On the Stability of Crystal Lattices. I. *Math. Proc. Cambridge Philos. Soc.* **1940**, *36* (2), 160−172.

(38) Frantsevich, I. N.; Voronov, F. F.; Bakuta, S. A. *Elastic Constants and Moduli of Elasticity of Metals and Nonmetals*; Naukova Dumka: Kiev, 1982.

(39) Pettifor, D. G. Theoretical Predictions of Structure and Related Properties of Intermetallics. *Mater. Sci. Technol. (United Kingdom)* **1992**, *8* (4), 345−349.

(40) Teter, D. M. Computational Alchemy: The Search for New Superhard Materials. *MRS Bull.* **1998**, *23* (1), 22−27.

(41) Tian, Y.; Xu, B.; Zhao, Z. Microscopic Theory of Hardness and Design of Novel Superhard Crystals. *Int. J. Refract. Met. Hard Mater.* **2012**, *33*, 93−106.

(42) Chen, X. Q.; Niu, H.; Li, D.; Li, Y. Modeling Hardness of Polycrystalline Materials and Bulk Metallic Glasses. *Intermetallics* **2011**, *19* (9), 1275−1281.

(43) Zhang, X.; Wang, X.; Li, F.; Zhou, Y. Mechanical and Thermal Properties of Antiperovskite Ti_3AlC Prepared by an In Situ Reaction/Hot-Pressing Route. *J. Am. Ceram. Soc.* **2009**, *92* (11), 2698−2703.

(44) Gaillac, R.; Pullumbi, P.; Coudert, F. X. ELATE: An Open-Source Online Application for Analysis and Visualization of Elastic Tensors. *J. Phys.: Condens. Matter* **2016**, *28* (27), 275201.

(45) Pierson, H. O. *Handbook of Refractory Carbides and Nitrides*; Noyes Publications: Westwood, NJ, 1996.

(46) HUME-ROTHERY, W. Elasticity and Anelasticity of Metals. *Nature* **1949**, *164* (4159), 84−85.

(47) Chung, D. H.; Buessem, W. R. The Elastic Anisotropy of Crystals. *J. Appl. Phys.* **1967**, *38* (5), 2010−2012.

(48) Ranganathan, S. I.; Ostoja-Starzewski, M. Universal Elastic Anisotropy Index. *Phys. Rev. Lett.* **2008**, *101* (5), 055504.

(49) Kube, C. M. Elastic Anisotropy of Crystals. *AIP Adv.* **2016**, *6* (9), 095209.

(50) Baughman, R. H.; Shacklette, J. M.; Zakhidov, A. A.; Stafstrom, S. Negative Poisson's ratios as a common feature of cubicmetals. *Nature* **1998**, *392*, 362−365.

(51) Li, C.; Chen, K.; Li, G.; Li, C.; Chen, Z. Elasticity, Anisotropy and Magnetism of Anti-perovskite M_3AlC (M = Ti, Fe, Sm) from First-Principle Calculations. *J. Supercond. Novel Magn.* **2018**, *31* (9), 2879−2887.

(52) Evarestov, R. A.; Bandura, A. V. First-Principles Calculations on the Four Phases of $BaTiO_3$. *J. Comput. Chem.* **2012**, *33* (11), 1123−1130.

(53) Hocine, H.; Amara, K.; Khelfaoui, F. Half-Metallic Stability of the Heusler Alloys TiZrIrZ (Z = Al, Ga, and In) under Volumetric Strain and Tetragonal Deformation. *Appl. Phys. A: Mater. Sci. Process.* **2020**, *126* (3), 1−10.

(54) Gao, Q.; Opahle, I.; Zhang, H. High-Throughput Screening for Spin-Gapless Semiconductors in Quaternary Heusler Compounds. *Phys. Rev. Mater.* **2019**, *3* (2), 1−12.

(55) Bunker, P. B.; Jensen, P. *Molecular Symmetry and Spectroscopy*; NRC Monograph Publishing Program: Ottawa, 2012.

(56) Tanveer Karim, A. M. M.; Hadi, M. A.; Alam, M. A.; Parvin, F.; Naqib, S. H.; Islam, A. K. M. A. Newly Synthesized $MgAl2Ge2$: A First-Principles Comparison with Its Silicide and Carbide Counterparts. *J. Phys. Chem. Solids* **2018**, *117*, 139−147.

(57) Pavlosiuk, O.; Kleinert, M.; Swatek, P.; Kaczorowski, D.; Wiśniewski, P. Fermi Surface Topology and Magnetotransport in Semimetallic LuSb. *Sci. Rep.* **2017**, *7* (1), 2−11.

(58) Qian, X.; Li, J.; Qi, L.; Wang, C. Z.; Chan, T. L.; Yao, Y. X.; Ho, K. M.; Yip, S. Quasiatomic Orbitals for Ab Initio Tight-Binding Analysis. *Phys. Rev. B* **2008**, *78* (24), 1−22.

(59) Dugdale, S. B. Life on the Edge: A Beginner's Guide to the Fermi Surface. *Phys. Scr.* **2016**, *91* (5), 053009.

(60) Li, S.; Ahuja, R.; Barsoum, M. W.; Jena, P.; Johansson, B. Optical Properties of Ti3SiC2 and Ti 4AlN3. *Appl. Phys. Lett.* **2008**, *92* (22), 221907.